I^{2}SIM: Boosting High-Fidelity Isotropic Super-Resolution with Image Interference and Spatial-Spectral Optimization

Enxing He[1], Yile Sun[1], Hongfei Zhu[2], Xinxun Yang[1], Lu Yin[3], Yubing Han[1*], Cuifang Kang[1,4,5*], Xu Liu[1,4,5]

[1]State Key Laboratory of Extreme Photonics and Instrumentation, College of Optical Science and Engineering, Zhejiang University, Hangzhou, 310027, Zhejiang, China.
[2]Department of Biomedical Engineering, The Chinese University of Hong Kong, Hong Kong, China.
[3]College of Optical and Electronic Technology, China Jiliang University, Hangzhou, 310018, Zhejiang, China.
[4]ZJU-Hangzhou Global Scientific and Technological Innovation Center, Hangzhou, 311200, Zhejiang, China.
[5]Collaborative Innovation Center of Extreme Optics, Shanxi University, Taiyuan, 030006, Shanxi, China.

*Corresponding author(s). E-mail(s): hanyubing@zju.edu.cn; cfkuang@zju.edu.cn;
Contributing authors: zjuenxinghe@gmail.com; yilesun@zju.edu.cn; hfzhu9927@link.cuhk.edu.hk; 22230022@zju.edu.cn; yinlu890622@163.com; liuxu@zju.edu.cn;

Abstract

Spatial resolution is crucial for imaging subcellular structures. The advent of three-dimensional structured illumination microscopy (3D-SIM) greatly benefits the biology community providing a powerful tool for imaging organelles with a two-fold resolution enhancement in all three dimensions. However, the axial resolution of 3D-SIM is limited to around 300 nm, which is inferior to its lateral resolution. Here we report a novel method, image interference SIM(I^{2}SIM), which utilizes two oppositely positioned objectives to detect fluorescence emission

interference based on three-beam excitation. By incorporating spectral modulation and spatial domain Frobenius Hessian optimization, I^2SIM achieves an axial resolution approximately twice that of 3D-SIM, reaching around 120 nm. Furthermore, we demonstrate the potential of I^2SIM through testing on various samples, including fluorescent beads, microtubules, and actin filaments.

Keywords: image interference, structured illumination microscopy, spatial-spectral optimization

1 Introduction

Observation of subcellular structures at high spatial resolution plays a crucial role in studying biological activities. Structured illumination microscopy(SIM) excites the sample with specific pattern, encodes high-frequency information into diffraction-limited passband and enhance the resolution through post-processing [1–4]. 3D-SIM introduces central illumination light to create variations in illumination structure along the axial direction and achieves a 2-fold enhancement of three-dimensional resolution. By employing various reconstruction algorithms [5–13], the quality of the image can be improved, leading to better optical sectioning. Thus it can reveal a multitude of biological mechanisms [14–17]. However, its axial resolution is still limited to around 300 nm.

In our previous work, an axial reconstruction accuracy of nearly 30 nm has been reported by employing fluorescence interference and multi-channel detection [18]. The axial information was calculated differently from SIM reconstruction, which poses an obstacle to its use on multilayered samples. Although it exhibits 30 nm axial resolution, its positioning in complex scenarios can be quite challenging. To achieve a conprehensive resolution enhancement, I^5S was proposed by employing six excitation beams for illumination and collecting fluorescence using two opposite objectives [19, 20]. It is able to reach an axial resolution of $\sim$ 100 nm. However, due to its intricate structured illumination field and complicated frequency shifts, its practical application is challenging. 4-beam SIM [21] simplified the acquisition set up using wide-field detection and put a mirror against the objective to generate 4-beam illumination. It can reach a 2-fold axial resolution improvement compared to 3D-SIM but still needs fine-tuning at the illumination end.

Here we propose a method using opposite objectives based on I^2M [22] and applying three excitation beams to avoid cumbersome adjustments at the illumination end. Inspired by Hessian-SIM [23, 24], joint spectral modulation and spatial domain Frobenius Hessian optimization are used to further enhance the imaging quality, eliminating artifacts and noises. In this way, axial resolution can be extended to $\sim$ 130 nm under 561 nm illumination Laser, remaining around 100 nm lateral resolution. We tested our method in fluorspheres, microtubules and actin filaments.

2 Results

2.1 Principle

The 4Pi configuration can naturally enhance the axial resolution in wide-field imaging because of the opposite objective setup. Through interference of fluorescence, the Optical transfer function (OTF) supporting region in the k_z axis can be extended from $[1 - cos(sin^{-1}(\mathrm{NA}/n))] \cdot nk_{em}$ to $2nk_{em}$, where NA denotes the numerical aperture, n is the refractive index of the immersion medium, and k_{em} is the wave vector of fluorescence in vacuum. To fill in the missing and low-value regions of the 4Pi OTF, we implemented structured illumination and spatial-spectral optimization. This approach resulted in a smoother and extended OTF, enabling the reconstructed image to achieve isotropically enhanced resolution and reduced artifacts. To achieve this, we used three beams to generate illumination pattern through one objective and detect the fluorescence through 4Pi configuration as shown in Fig. 1a. On the right side of Fig. 1a, the theoretical 4Pi PSF generated using vectorial diffraction theory which has side lobes [25] are shown and its profile when the phase difference between two optical path through opposite objective is 0. The 4Pi wide-field OTF is obtained using 3D fast Fourier Transform, and its augmented density is calculated as $log(|\cdot| + 1)$. The center of OTF has zero points and the side has low-value points.

An important part in I^2SIM is the reconstruction after obtaining raw images. Here we applied Open-3DSIM [26] as framework and adjusted it to suit 4Pi imaging. The pipeline is shown in Fig. 1b. First an image stack is collected with 15 raw images of 3D SIM for each layer. A simulated 4Pi OTF is used to build frequency domain filters, which include $filter_1$ and $filter_2$. Specifically, $filter_1 = \frac{Apo}{OTF_{notch}+w_1^2}$, $filter_2 = \frac{Apo}{OTF_{notch}+w_2^2}$, where Apo is the apodization function in the 3D frequency domain. w_1 and w_2 are the parameters to design filters, repectively. The OTF_{notch} can be constructed as: $OTF_{notch} = \sum_{n=-2}^{2} m(n) \cdot OTF(n) \cdot notch(n)$, where $notch(n)$ and $OTF(n)$ are the notch-filter and leaky-cone-shaped optical transfer function shifted to the n-th place in the frequency domain. $m(n)$ is the weight coefficient of different Fourier orders. The filters are applied to the directly-combined SIM spectrum to suppress spectral side lobes, thereby reducing artifacts and enhancing the quality of reconstruction.

$$\tilde{f} = \tilde{f}_{SR} \cdot filter_1 \cdot filter_2, \tag{1}$$

where $\tilde{f}_{SR}$ is the directly combined SIM spectrum and $\tilde{f}$ is the final SIM spectrum output of open-3DSIM with artifacts. Although filters can increase resolution and surpass noise and side lobes, there still exist artifacts and noises due to the unsmooth synthetic OTF. To solve this problem, space-domain optimization using frobenius norm of Hessian and l_1 norm as regularization is applied. Upon finishing SIM reconstruction, we can construct the following loss function:

$$\underset{f}{argmin}\{\frac{1}{2}\|Hf - b\|_2^2 + \lambda_1\|f\|_1 + \lambda_2\|Hessian_{Frob}(f)\|_1\} \tag{2}$$

The operator H is a binary frequency mask which shares the same region as reconstructed effective OTF to make sure the fidelity is considered only in physically

detected area. $\|\cdot\|_1$ and $\|\cdot\|_2$ are l_1 and l_2 norms, respectively. l_1 norm guarantees the sparsity and frobenius norm of Hessian recovers the continuity of sample with better ISNR [27], respectively. The frobenius norm of Hessian can be represented as:

$$Hessian_{Frob}(f) = \sqrt{f_{xx}^2 + 2f_{xy}^2 + f_{yy}^2 + 2\lambda_z f_{xz}^2 + 2\lambda_z f_{yz}^2 + \lambda_z^2 f_{zz}^2} \tag{3}$$

Here $f_{xx} = \partial^2 f/\partial x^2$, and similar operations are performed for the others. λ_1, λ_2, and λ_z adjust the weights of various terms, balancing fidelity and regularization. By optimizing the loss function using Alternating Direction Method of Multipliers(ADMM) iteratively which is further discussed in Methods, the recovered OTF will have a more uniformly extended supporting region than ordinary 3D-SIM as shown in Fig. 1c, ensuring ideal reconstruction quality.

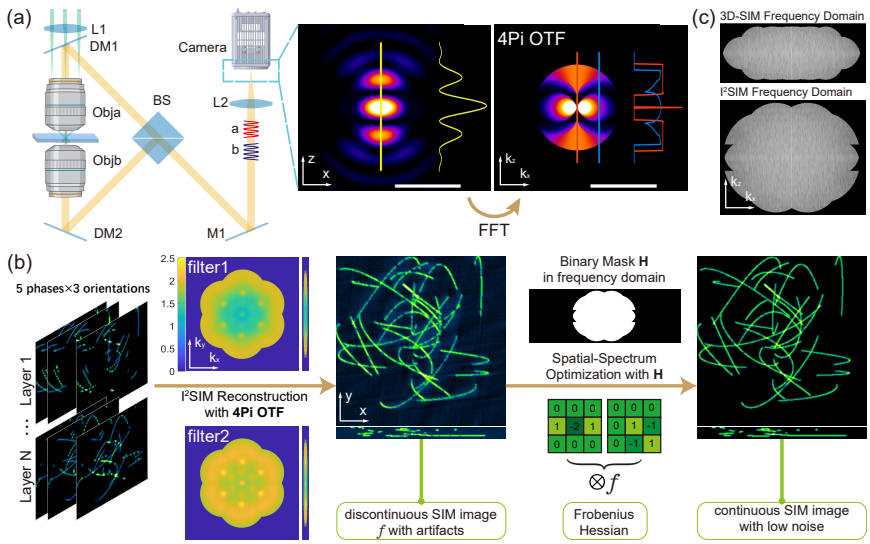

Fig. 1 Principle of I^{2}SIM. (a) (Left)Structure schematic diagram of 4Pi-SIM. The sample is illuminated by three beams the same as 3D-SIM through one objective and fluorescence detected by both objectives will interfere with each other on CMOS; (Middle)4Pi PSF on CMOS; (Right)The corresponding OTF. Line profile of PSF is normalized and Profiles of OTF were calculated by normalized $log(abs(Intensity) + 1)$. (b) Algorithm flow. (c) Comparison of OTF supporting region between 3D-SIM and I^{2}SIM.

2.2 Simulation and Calibration

Simulated randomly three-dimensionally distributed fluorspheres and microtubules were used to verify the effectiveness of the method. Fluorspheres were generated as points of no diameter and then convolved by wide-field PSF and 4Pi PSF with 0 phase difference. Because of 0 nm diameter, the reconstructed result can reflect real resolution. The PSF was generated using the method mentioned before with 1.45 NA

objective and 1.518 refractive index. After reconstruction, x-y pixel size was interpolated to 41.8 nm and z axis was not interpolated. The axial range was from -800 nm to 800 nm which means there were 31 layers. As shown in Fig. 2a, our method shared same lateral resolution with 3D-SIM. The axial resolution of wide-field, open-3DSIM and I^2SIM were compared on the right side of Fig. 2a, axial distributions of fluorspheres were dramatically decreased and OTF supporting area's max value was extended from $\sim 1.4k_{em}$ to $\sim 2.7k_{em}$. The full-width at half-maximum(FWHM) values for wide-field, open3D-SIM, and I^2SIM are 497.1 nm, 284.4 nm and 133.0 nm under center emission wavelength of 590 nm, respectively. Simulated microtubules were also reconstructed to test the performance under the same imaging parameters as fluorspheres. The pixel number was 301 laterally and 21 axially. The upper row of Fig. 2 is a middle slice comparing three methods. It is worth noting that, although 3D-SIM and I^2SIM share the same lateral resolution, our approach exhibits fewer artifacts in each slice. This improvement is attributed to the higher axial resolution, which mitigates the influence of adjacent slices, showing clearer axial structures (Fig. 2c).

We also examined reconstruction performance on high-density 100 nm Fluorsphere sample (FluoSpheres beads, F8801) under 561 nm excitation wavelength. One slice in x-z plane is depicted(Fig. 2d). As expected, our method maintained the ∼2-fold lateral resolution enhancement of 3D-SIM over wide-field microscopy while offering ∼2-fold-better axial resolution than 3D-SIM. We counted 76 beads for wide-field, 100 beads for 3D-SIM, and 100 beads for I^2SIM, and plotted their box plots(Fig. 2. Their average FWHM were 633.7 nm, 302.3 nm, and 178.4 nm, respectively. Taking into account the size of the beads, this result is in line with our expectations.

2.3 Cell Imaging

To verify the performance of our methodI^2SIM in applications, we used it to observe several cell samples in which the imaging condition was more complicated. Fixed microtubule networks of BSC cells labeled with Abberior STAR red were first tested(Fig. 3). The 3D illumination pattern was generated by 647 nm Laser and centered at the focal plane of both objective lenses. We collected 15 images(5 phases per orientation × 3 orientation) for each layer and then moved z-piezo stage to achieve axial scanning every 50 nm interval to focus on another layer.

Depth-encoded images revealed that microtubules were primarily concentrated in the upper layer of the photographed area. Furthermore, the enlarged view confirmed that our approach matched the lateral resolution of 3D-SIM and experienced reduced axial interference(Fig. 3a). In axial view, wide-field microscopy could barely discern the closely spaced microtubules, the intervals of which were more distinctly visible in 3D-SIM. However, by employing I^2SIM, structures with a spacing of 200 nm can be clearly resolved, underscoring the ability of 4Pi detection to unveil axial detail otherwise masked by diffraction(Fig. 3b, c).

The effectiveness of the algorithm was also tested. By employing frequency domain filters in the open3D-SIM reconstruction process, side-lobes were surpassed, resulting in structures with clearer edges and enhanced resolution. l_1 norm was used to further mitigate noise and improve the resolution, but it can lead to discontinuities in

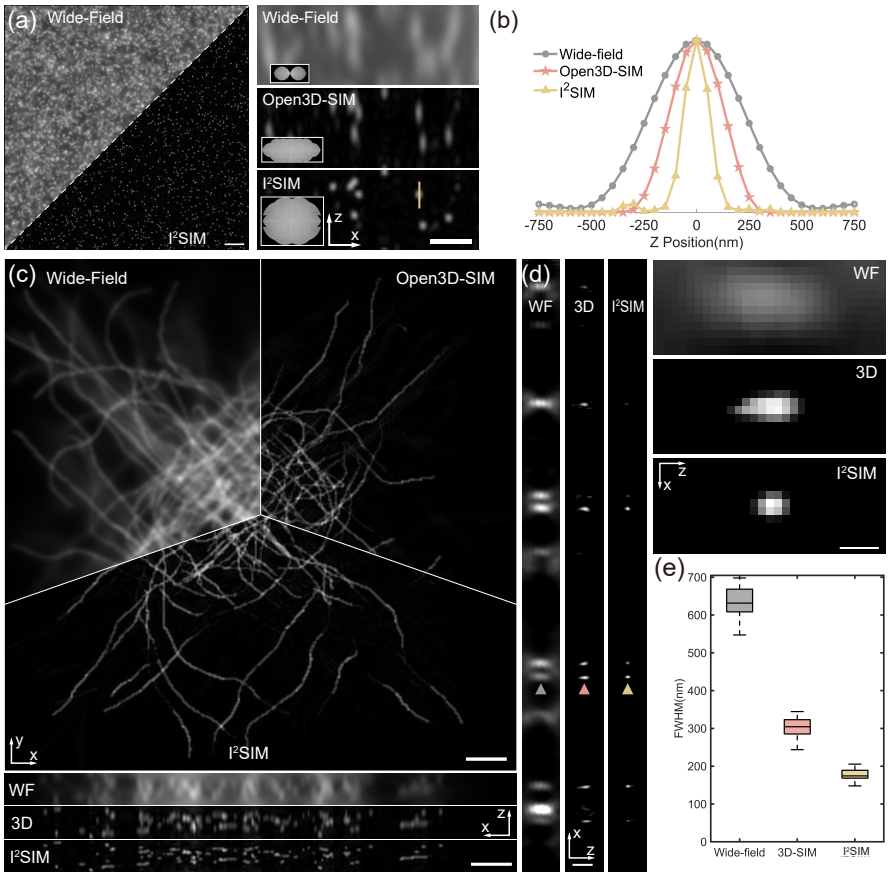

Fig. 2 Simulation and beads experiment. (a)(Left)One layer of simulated beads reconstruction result; (Right)Axial cross-sectional views of simulated beads. Insets show magnitude of OTFs(k_x/k_zplane) derived from images. (b)Line profiles corresponding to bead images shown in the right side of (a), taken along vertical line in (a). (c)Reconstruction results of simulated microtubules, including the comparison of the wide-field, open3D-SIM and our method. (d)(Left)One layer of reconstruction results of 100 nm beads in x-z plane; (Right)Higher magnification views of bead highlighted by colored arrowheads in Left. (e)Quantification of axial FWHM for n = 76, 100 and 100 beads for wide-field microscopy, 3D-SIM and I^2SIM, respectively.Whiskers: maximum and minimum; center lines: medians; bounds of box: 75th and 25th percentiles. Scale bars, 2 μm in(a)(Left), 800 nm in (a)(Right), 2 μm in (c), 800 nm in (d)(Left), 250 nm in (d)(Right).

the structure. The purpose of the frobenius Hessian norm was to correct these discontinuities without losing much resolution, achieving an improvement in image quality with isotropic properties(Fig. 3d). Profiles perpendicular to the direction of the structure(Fig. 3e1) demonstrate the suppression of noise and the preservation of resolution, while profiles along the direction of the structure(Fig. 3e2) show a smoothing of intensity variations and an enhancement of continuity. By demonstrating several slices in layer stack(Fig. 3f), the orientation and spatial distribution of microtubule growth can be observed. The nearer to the cell center, the microtubule distribution was closer to the upper layer, showing an upward trend.

Next we tested method on actin filaments of U2OS cells labeled with actin-555(Fig. 4a). Here, whether in the y-z view where profiles were alighted with the structural direction(Fig. 4b, d), or in the x-z view where profiles were perpendicular to the structural direction(Fig. 4c, e), the axial resolution was enhanced.

3 Discussion

In order to achieve high-quality imaging, there are several factors that need to be considered: (1)the size of field of view; (2)the aberration correction of system; (3)the selection of reconstruction parameters. As shown in Results section, the field of view(FOV) we used is 25.163 $\mu m \times 25.163$ μm, which only had a pixel size of 301×301. If FOV is expanded, the 4Pi PSF at the periphery of the field will differ from that at the center, because of the varying optical path differences at the edge. This results in the imaging target being only a part of the cell's structure, preventing high-throughput imaging. By introducing vectorial PSF phase retrieval [28, 29] in separate regions, this problem can be improved. Additionally, fluorescent interference is highly sensitive to aberrations, which can lead to the deformation of the PSF and, consequently, distorted results. Here we used adaptive optics, typically deformable mirrors [30], to address this problem. Although there was still a slight tilt in the PSF, it can have little influence on the quality of the reconstruction.

4 Conclusion

In summary, we report I^2SIM, a powerful approach to enhance axial resolution in imaging subcellular structures and morphologies of cells, which improves the axial resolution to ~ 130 nm, about 2-fold improvement compared with 3D-SIM and maintains the lateral resolution of 3D-SIM at the same time. Using this approach, the fine axial structures that are originally difficult to discern in traditional SIM can now be resolved, enhancing the optical sectioning capability.

To overcome the non-uniformity of synthetic OTF in SIM reconstruction, which tends to cause artifacts and noises, a space-domain optimization was developed based on sparsity(l_1 norm) and continuity(frobenius Hessian norm). They can suppress the background and noise and meanwhile slightly enhance isotropic resolution. By employing the ADMM algorithm for iteration, rapid convergence can be achieved. Our method makes a balance between resolution and acquiring speed, by adding new illumination pattern like 4-beam interference and new algorithm like deep learning, it's limitations can be overcome in the future.

5 Methods

5.1 Details of optimization algorithm

We adopted ADMM to solve the optimization problem in Eq. (2).Scaled ADMM was employed for simplicity. The Augmented Lagrangian function was constructed as:

$$\begin{aligned} L =& \frac{1}{2}\|Hf-b\|_2^2 + \lambda_1\|d_1\|_1 + \\ & \lambda_2\|\sqrt{d_{xx}^2+d_{xy}^2+d_{yy}^2+d_{xz}^2+d_{yz}^2+d_{zz}^2}\|_1 + \\ & \sum_{\text{for all } d}\left[\frac{\rho}{2}\|Af-d+\omega\|_2^2 - \frac{\rho}{2}\|\omega\|_2^2\right]. \end{aligned} \tag{4}$$

For each $d(d_1,\ d_{xx},\ d_{xy},\ d_{yy},\ d_{xz},\ d_{yz},\ d_{zz})$, there is one A operator and one scaled dual variable ω. A is in the form of $I,\ \nabla_{xx},\ \sqrt{2}\nabla_{xy},\ \nabla_{yy},\ \sqrt{2\lambda_z}\nabla_{xz},\ \sqrt{2\lambda_z}\nabla_{yz},\ \lambda_z\nabla_{zz}$, respectively. Here, I denotes an identity matrix of the same size as the input image stack, and operator ∇ represents the second-order partial derivative operation on the image stack indicated by its subscripts.

By minimizing L with respect to f, d, and ω iteratively, the best value of f can be found. Take the partial derivative of L with respect to f and set it equal to zero, we can get:

$$\frac{\partial L}{\partial f} = H^T(Hf-b) + \sum_{\text{for all } d}\left[\rho A^T(Af-d+\omega)\right] = 0. \tag{5}$$

$\cdot^T$ denotes the transpose of a matrix. f can be extracted and solved using the Fourier Transform(Eq. (6)).

$$f^{i+1} = ifftn\left[\frac{\sum_{\text{for all } d}\tilde{A}^* \odot (\tilde{d}^i - \tilde{\omega}^i) + \frac{\tilde{H}^* \odot \tilde{b}}{\rho}}{\sum_{\text{for all } d}|\tilde{A}|^2 + \frac{|\tilde{H}|^2}{\rho}}\right], \tag{6}$$

$\tilde{\cdot}$ is the Fourier Transform of matrix, $\cdot^*$ represents the conjugate of complex matrix, and $\odot$ denotes element-wise multiplication.

Next we update each d through the same way as f, for all d except d_1, the partial derivative of L is calculated(Eq. (7)).

$$\frac{\partial L}{\partial d} = \frac{\lambda_2 d}{\sqrt{d_{xx}^2+d_{xy}^2+d_{yy}^2+d_{xz}^2+d_{yz}^2+d_{zz}^2}} + \rho(d-C^i) = 0 \tag{7}$$

$$\begin{cases} C_{xx}^i = \nabla_{xx} f^{i+1} + \omega_{xx}^i \\ C_{xy}^i = \sqrt{2}\nabla_{xy} f^{i+1} + \omega_{xy}^i \\ C_{yy}^i = \nabla_{yy} f^{i+1} + \omega_{yy}^i \\ C_{xz}^i = \sqrt{2\lambda_z}\nabla_{xz} f^{i+1} + \omega_{xz}^i \\ C_{yz}^i = \sqrt{2\lambda_z}\nabla_{yz} f^{i+1} + \omega_{yz}^i \\ C_{zz}^i = \lambda_z \nabla_{zz} f^{i+1} + \omega_{zz}^i \end{cases}$$

Since the d's are coupled, we need to find the multivariate function extremum of L with respect to d. When the six equations derived from Eq. 6 are combined, the following relationships are obtained:

$$\frac{d_{xx}}{C_{xx}} = \frac{d_{xy}}{C_{xy}} = \frac{d_{yy}}{C_{yy}} = \frac{d_{xz}}{C_{xz}} = \frac{d_{yz}}{C_{yz}} = \frac{d_{zz}}{C_{zz}}. \tag{8}$$

Take d_{xx} as example, substituting the above conclusions(Eq. 8) back into Eq. 7, we can obtain:

$$\frac{\lambda_2 d_{xx}}{\sqrt{\sum_{\text{for all } C} \left(\frac{d_{xx}}{C_{xx}} C\right)^2}} + \rho(d_{xx} - C_{xx}) = 0, \tag{9}$$

which can be simplified to:

$$\frac{\lambda_2 \cdot sign(d_{xx})|C_{xx}|}{\sqrt{\sum_{\text{for all } C} (C)^2}} + \rho(d_{xx} - C_{xx}) = 0. \tag{10}$$

Here, $sign(d)$ is 1 when $d > 0$, -1 when $d < 0$, and 0 when $d = 0$. Through classification discussion, the iterative formula for d_{xx} can be summarized as a soft-threshold function:

$$d_{xx}^{i+1} = \begin{cases} C_{xx}^i - |C_{xx}^i| \frac{\lambda_2/\rho}{\sqrt{\sum(C)^2}}, & C_{xx}^i > |C_{xx}^i| \frac{\lambda_2/\rho}{\sqrt{\sum(C)^2}} \\ 0, & -|C_{xx}^i| \frac{\lambda_2/\rho}{\sqrt{\sum(C)^2}} < C_{xx}^i < |C_{xx}^i| \frac{\lambda_2/\rho}{\sqrt{\sum(C)^2}} \\ C_{xx}^i + |C_{xx}^i| \frac{\lambda_2/\rho}{\sqrt{\sum(C)^2}}, & C_{xx}^i < -|C_{xx}^i| \frac{\lambda_2/\rho}{\sqrt{\sum(C)^2}} \end{cases} \tag{11}$$

Similar operations can be applied to the iteration of other d's (except d_1). By considering case when $d = 0$, Eq. 11 can be transformed into a more general form:

$$d_{xx}^{i+1} = max\left(\sqrt{\sum (C^i)^2} - \frac{\lambda_2}{\rho}\right) \odot \frac{C_{xx}^i}{\sqrt{\sum (C^i)^2}}. \tag{12}$$

For d_1, it is easy to derive the iteration formula of d_1, which is also a soft-threshold function:

$$d_1^{i+1} = S_{\frac{\lambda_1}{\rho}}(f^{i+1} + \omega^i), \tag{13}$$

where $S_\gamma(y) = max(y - \gamma, 0) + min(y + \gamma, 0)$. For all ω, the iterations are similar, which can be denoted as:

$$w^{i+1} = w^i + Af^{i+1} - d^{i+1} \tag{14}$$

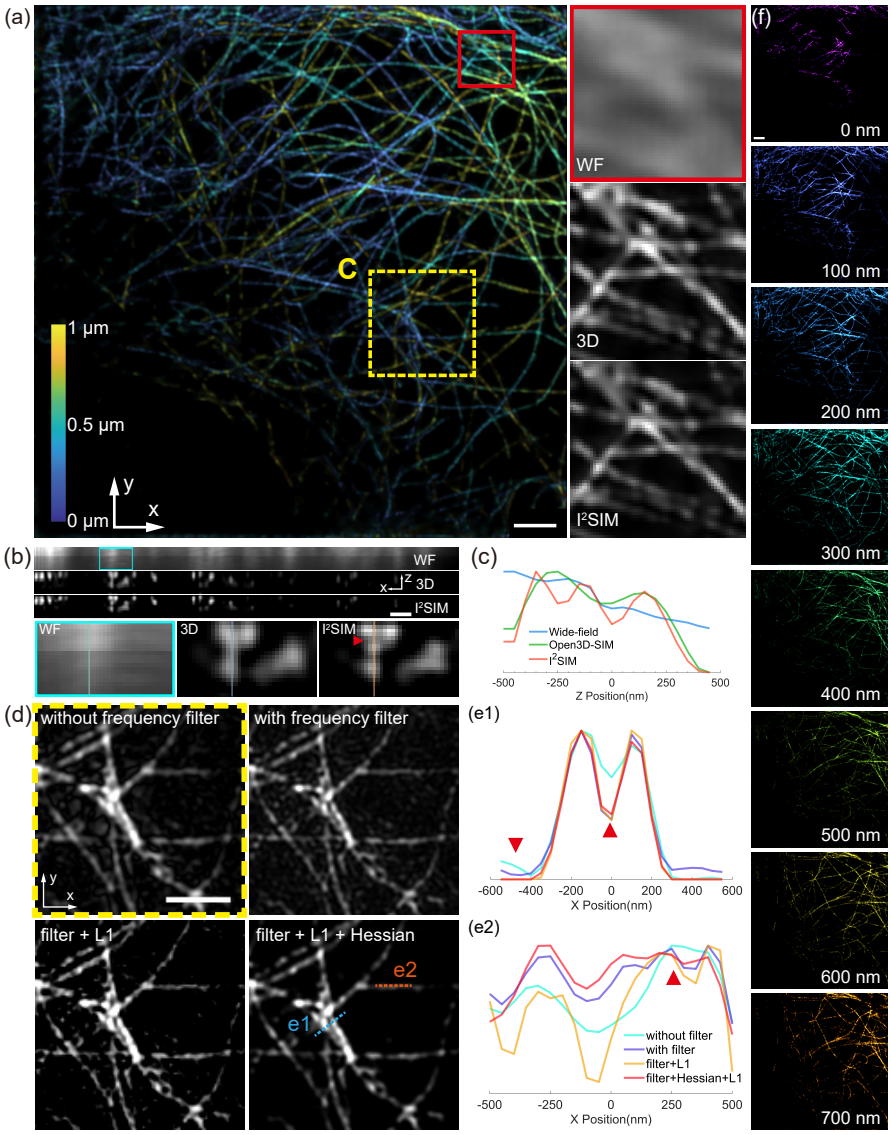

Fig. 3 I^{2}SIM enables near-isotropic imaging of microtubules. (a) (Left)Maximum intensity projection of fixed BSC cells labeled with the Abberior STAR Red. Image is depth coded as indicated; (Right)Higher magnification lateral views(single planes) corresponding to red rectangle in (Left) are shown, comparing wide-field microscopy(upper), 3D-SIM(middle) and 4Pi-SIM(lower). (b) (Top)Axial cross-sectional views of microtubules in (a); (Middle)Higher magnification views corresponding to rectangle indicated in the wide-field (WF) image at the top. (c)Line profiles corresponding to vertical line in (b). (d) Higher magnification lateral views corresponding to yellow dashed rectangle in (a), comparing unmodified image, frequency-filtered image, image modified by frequency filter and sparsity regularization, and image modified by frequency filter and sparsity plus Frobenius Hessian regularization. (e)Line profiles taken along dashed line e1 and e2 in (d). (f)Continuous x-y section of the 3D volume from 0 to 700 nm depth with a 100-nm axial interval, illustrating the changing morphology of microtubule networks. Scale bars, 2 μm (a, f); 1 μm (b); 1.5 μm (d).

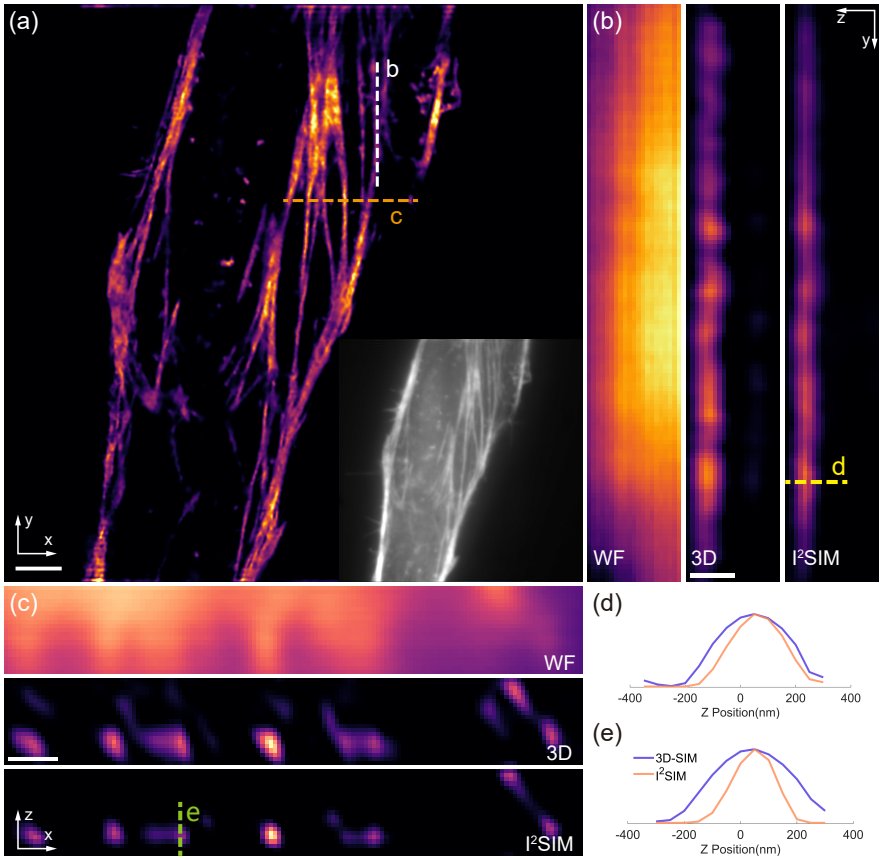

Fig. 4 I^2SIM enables the enhancement of axial resolution for actin filaments. (a)Single lateral plane of actin filaments in U2OS labeled with actin-555. (b)Axial views corresponding to white dashed line in (a), comparing wide-field microscopy(WF), 3D-SIM(3D), I^2SIM. (c)Axial views corresponding to orange dashed line in (a), comparing wide-field microscopy(WF), 3D-SIM(3D), I^2SIM. (d)Line profiles corresponding to yellow dashed line in (b). (e)Line profiles corresponding to green dashed line in (c). Scale bars, 2 μm (a); 500 nm (b,c).

The pseudo code is as follows:

Algorithm 1 Frobenius Hessian Sparsity Optimization

Input: f^0, H, λ_1, λ_2, λ_z, ρ, IterNum
Output: de-noised image stack f^* with depressed artifacts

```
Initialize:
all d, ω ← f^0.
for i = 0 to IterNum-1 do
    Update f^{i+1} according to Eq. 6.
    Update d_1^{i+1} according to Eq. 13.
    Update d_xx^{i+1}–d_zz^{i+1} according to Eq. 12.
    Update all ω^{i+1} according to Eq. 14.
end for
f* ← f^{IterNum}
```

5.2 Data acquisition and reconstruction

The reason we chose a 50 nm layer interval was to comply with the Nyquist sampling theorem, given that the theoretical axial resolution is approximately 130 nm. Taking into account the thickness of the cells and the range of microtubules, the number of scanning layers was set to 21. This allows for the reconstruction of the structure of the important layers with minimal information loss while also maintaining the speed of reconstruction.

The selection of reconstruction parameters play a crucial role in the outcome of the reconstruction [31]. For open3D-SIM algorithm, we mainly adjusted the notch depth of $filter_1$ and $filter_2$, to surpass the background noise and at meanwhile maintain signals. With a good outcomes of SIM reconstruction, the following optimization will have a better performance. The parameters in the last step decide whether the optimization can converge and reach the best solution. λ_1 determines the sparsity of the results. The larger its value, the more noise is suppressed, the more discontinuous the structures become, and the sharper the edges are. λ_2 determines the significance of frobenius Hessian norm, enhance the continuity of samples at the sacrifice of resolution. Correct configuration allows for resolution to be maintained or even slightly enhanced when noise and artifacts are mitigated. This needs repeated trials, which is a drawback of the algorithm. For separated samples like beads, λ_1 ought to be large and for continuous samples like microtubules and actin filaments, a larger λ_2 will be appropriate. λ_z controls the importance of axial continuity, most of time it is set to 1 for an isotropic result.

When the sample is discrete and not continuous enough such as fluorspheres, we adopted aggressive choice of reconstruction parameters. In the reconstruction process of open-3DSIM, we set the notch depth to 0.96 for $filter_1$ and 0.98 for $filter_2$ in order to achieve a balance between enhancing resolution and preserving signal integrity. For the optimization step, $lambda_1$ was 0.05, $lambda_2$ was 0.005, and $lambda_z$ was 1.

A large $lambda_1$ and small $lambda_2$ make the result sparser. When sample is continuous structures like microtubules(Fig. 3) and actin filaments(Fig. 4), We tend to choose more conservative reconstruction parameters. In the open3D-SIM reconstruction process, we set the notch depth to 0.96 for $filter_1$ and 0.98 for $filter_2$. For the optimization step, $lambda_1$ was 0.03, $lambda_2$ was 0.01, and $lambda_z$ was 1 to get a more continuous results.

5.3 Sample preparation

25 mm diameter round precision glass coverslips (Thorlabs) were immersed in ultrapure water and vibrated in an ultrasonic cleaner for 15 minutes. Coverslips were sterilized using 95% ethanol. BSC were purchased from the American Type Culture Collection and cultured in Minimum Essential Media (MEM; Thermo Fisher Scientific, Inc.) supplemented with 10% (v/v) fetal bovine serum (FBS; Thermo Fisher Scientific, Inc.). U2OS were cultured in McCoy's 5A Media (Thermo Fisher Scientific, Inc.) supplemented with 10% FBS. Cultures were maintained at 37 °C in a humidified environment containing 5% CO_2.

For bead samples, we used red fluorescent FluoSpheres beads (F8801) for fluorescent bead samples, which were maximally excited at 589 nm. Dilute the beads in ultrapure water at a ratio of 1:10, and vibrate in an ultrasonic cleaner for 5 min. Next, 200 μl of the diluted beads were placed on a coverslip and allowed to stand for 10 min. The absorbent tissue was then used to remove excess water and Prolong Glass Antifade (Thermo Fisher Scientific, Inc.) before sealing the coverslip.

For the immunolabeling of microtubules, BSC cells were seeded into the prepared coverslips. After overnight incubation, the cells were washed thrice with phosphate-buffered saline (PBS, Thermo Fisher Scientific, Inc.), fixed with 3% (m/v) paraformaldehyde (PFA, Electron Microscopy Sciences) and 0.1% (v/v) glutaraldehyde (GA, SigmaAldrich Co., LLC) for 13 minutes at 37 °C, and quenched with NaHB4 for 7 minutes at room temperature (RT). The cells were incubated with 0.2% (v/v) Triton X-100 (Sigma-Aldrich Co., LLC) and 5% goat serum (Thermo Fisher Scientific, Inc.) for 1 hour at RT. Microtubules were stained with mouse alpha and beta tubulin antibodies (WA31679510 and TG2597441, Invitrogen) at 1:1:200 dilution in PBS overnight at 4 °C and goat anti-mouse STAR Red (Abberior GmbH) at 1:200 dilution in PBS for 1 hour. Samples were washed three times with PBS before imaging, with two washes for 3 minutes and the last wash for 15 minutes.

To label the actin filaments in U2OS cells, the cells were seeded onto the prepared coverslips. After overnight incubation, the cells were washed thrice with PBS. Next, the cells were fixed with 3% PFA and 0.1% GA in PBS for 13 minutes and then rinsed three times with PBS. Subsequently, the cells were incubated with Actin-555(Thermo Fisher Scientific, Inc.) diluted at concentration of 1.5:200 for 30 minutes at room temperature. The cells were then washed three times with PBS and stored in PBS at 4 °C until imaged, with two washes for 3 minutes and the last wash for 15 minutes.

Acknowledgements. Acknowledgements are not compulsory. Where included they should be brief. Grant or contribution numbers may be acknowledged.

Please refer to Journal-level guidance for any specific requirements.

Funding. This work was financially sponsored by the National Natural Science Foundation of China (62125504, 62361166631); STI 2030—Major Projects (2021ZD0200401); the Fundamental Research Funds for the Central Universities (2022FZZX01-20).

Declarations

Competing interests. The authors declare that they have no competing interests.

References

[1] Gustafsson, M.G.L.: Surpassing the lateral resolution limit by a factor of two using structured illumination microscopy. Journal of Microscopy **198**(2), 82–87 (2000) https://doi.org/10.1046/j.1365-2818.2000.00710.x

[2] Gustafsson, M.G.L., Shao, L., Carlton, P.M., Wang, C.J.R., Golubovskaya, I.N., Cande, W.Z., *et al.*: Three-dimensional resolution doubling in wide-field fluorescence microscopy by structured illumination. Biophysical Journal **94**(12), 4957–4970 (2008) https://doi.org/10.1529/biophysj.107.120345

[3] Shao, L., Kner, P., Rego, E.H., Gustafsson, M.G.L.: Super-resolution 3d microscopy of live whole cells using structured illumination. Nature Methods **8**(12), 1044–1046 (2011) https://doi.org/10.1038/nmeth.1734

[4] Chen, X., Zhong, S., Hou, Y., Cao, R., Wang, W., Li, D., *et al.*: Super-resolution structured illumination microscopy reconstruction algorithms: A review. Light: Science & Applications **12**(1), 172 (2023) https://doi.org/10.1038/s41377-023-01204-4

[5] Zhu, H., Sun, Y., Yin, L., Han, J., Cai, M., Liu, Q., Kuang, C., Hao, X., Liu, X.: 3d super-resolution microscopy based on nonlinear gradient descent structured illumination. Optics Express **29**(14), 21428 (2021) https://doi.org/10.1364/OE.424740

[6] Cai, M., Zhu, H., Sun, Y., Yin, L., Xu, F., Wu, H., Hao, X., Zhou, R., Kuang, C., Liu, X.: Total variation and spatial iteration-based 3d structured illumination microscopy. Optics Express **30**(5), 7938–7953 (2022) https://doi.org/10.1364/OE.451190

[7] Wen, G., Li, S., Liang, Y., Wang, L., Zhang, J., Chen, X., Jin, X., Chen, C., Tang, Y., Li, H.: Spectrum-optimized direct image reconstruction of super-resolution structured illumination microscopy. PhotoniX **4**(1), 19 (2023) https://doi.org/10.1186/s43074-023-00092-6

[8] Wen, G., Li, S., Wang, L., Chen, X., Sun, Z., Liang, Y., Jin, X., Xing, Y., Jiu, Y., Tang, Y., Li, H.: High-fidelity structured illumination microscopy by point-spread-function engineering. Light: Science & Applications **10**(1), 70 (2021) https:

//doi.org/10.1038/s41377-021-00513-w

[9] Qian, J., Xu, K., Feng, S., Liu, Y., Ma, H., Chen, Q., Zuo, C.: Fast-structured illumination microscopy based on dichotomy–correlation parameter estimation (dcor-sim). ACS Photonics (2024) https://doi.org/10.1021/acsphotonics.3c01845

[10] Cao, R., Chen, Y., Liu, W., Zhu, D., Kuang, C., Xu, Y., Liu, X.: Inverse matrix based phase estimation algorithm for structured illumination microscopy. Biomedical Optics Express **9**(10), 5037–5051 (2018) https://doi.org/10.1364/BOE.9.005037

[11] Wicker, K., Mandula, O., Best, G., Fiolka, R., Heintzmann, R.: Phase optimisation for structured illumination microscopy. Optics Express **21**(2), 2032–2049 (2013) https://doi.org/10.1364/OE.21.002032

[12] Qian, J., Cao, Y., Bi, Y., Wu, H., Liu, Y., Chen, Q., Zuo, C.: Structured illumination microscopy based on principal component analysis. eLight **3**(1), 4 (2023) https://doi.org/10.1186/s43593-022-00035-x

[13] Wang, Z., Zhao, T., Hao, H., Cai, Y., Feng, K., Yun, X., Liang, Y., Wang, S., Sun, Y., Bianco, P.R., Oh, K., Lei, M.: High-speed image reconstruction for optically sectioned, super-resolution structured illumination microscopy. Advanced Photonics **4**(2), 026003 (2022) https://doi.org/10.1117/1.AP.4.2.026003

[14] Strauss, M.P., Liew, A.T.F., Turnbull, L., Whitchurch, C.B., Monahan, L.G., Harry, E.J.: 3d-sim super resolution microscopy reveals a bead-like arrangement for ftsz and the division machinery: Implications for triggering cytokinesis. PLOS Biology **10**(9), 1001389 (2012911) https://doi.org/10.1371/journal.pbio.1001389

[15] Rowlett, V.W., Margolin, W.: 3d-sim super-resolution of ftsz and its membrane tethers in *escherichia coli* cells. Biophysical Journal **107**(8), 17–20 (2014) https://doi.org/10.1016/j.bpj.2014.08.024

[16] Cogger, V.C., McNerney, G.P., Nyunt, T., DeLeve, L.D., McCourt, P., Smedsrød, B., Le Couteur, D.G., Huser, T.R.: Three-dimensional structured illumination microscopy of liver sinusoidal endothelial cell fenestrations. Journal of Structural Biology **171**(3), 382–388 (2010) https://doi.org/10.1016/j.jsb.2010.06.001

[17] Rodermund, L., Coker, H., Oldenkamp, R., Wei, G., Bowness, J., Rajkumar, B., Nesterova, T., Susano Pinto, D.M., Schermelleh, L., Brockdorff, N.: Time-resolved structured illumination microscopy reveals key principles of xist rna spreading. Science **372**(6547), 7500 (2021) https://doi.org/10.1126/science.abe7500

[18] Sun, Y., Zhu, H., Yin, L., Wu, H., Cai, M., Sun, W., *et al.*: Fluorescence interference structured illumination microscopy for 3d morphology imaging with high axial resolution. Advanced Photonics **5**(5), 056007 (2023) https://doi.org/10.1117/1.AP.5.5.056007

[19] Shao, L., Isaac, B., Uzawa, S., Agard, D.A., Sedat, J.W., Gustafsson, M.G.L.: I5s: Wide-field light microscopy with 100-nm-scale resolution in three dimensions. Biophysical Journal **94**(12), 4971–4983 (2008) https://doi.org/10.1529/biophysj.107.120352

[20] Shao, L., Winoto, L., Agard, D.a., Gustafsson, M.g.l., Sedat, J.w.: Interferometer-based structured-illumination microscopy utilizing complementary phase relationship through constructive and destructive image detection by two cameras. Journal of Microscopy **246**(3), 229–236 (2012) https://doi.org/10.1111/j.1365-2818.2012.03604.x

[21] Li, X., Wu, Y., Su, Y., Rey-Suarez, I., Matthaeus, C., Updegrove, T.B., *et al.*: Three-dimensional structured illumination microscopy with enhanced axial resolution. Nature Biotechnology **41**(9), 1307–1319 (2023) https://doi.org/10.1038/s41587-022-01651-1

[22] Gustafsson, Agard, Sedat: I5m: 3d widefield light microscopy with better than 100 nm axial resolution. Journal of Microscopy **195**(1), 10–16 (1999) https://doi.org/10.1046/j.1365-2818.1999.00576.x

[23] Huang, X., Fan, J., Li, L., Liu, H., Wu, R., Wu, Y., *et al.*: Fast, long-term, super-resolution imaging with hessian structured illumination microscopy. Nature Biotechnology **36**(5), 451–459 (2018) https://doi.org/10.1038/nbt.4115

[24] Zhao, W., Zhao, S., Li, L., Huang, X., Xing, S., Zhang, Y., *et al.*: Sparse deconvolution improves the resolution of live-cell super-resolution fluorescence microscopy. Nature Biotechnology **40**(4), 606–617 (2022) https://doi.org/10.1038/s41587-021-01092-2

[25] Lang, M.C., Staudt, T., Engelhardt, J., Hell, S.W.: 4pi microscopy with negligible sidelobes. New Journal of Physics **10**(4), 043041 (2008) https://doi.org/10.1088/1367-2630/10/4/043041

[26] Cao, R., Li, Y., Chen, X., Ge, X., Li, M., Guan, M., *et al.*: Open-3dsim: An open-source three-dimensional structured illumination microscopy reconstruction platform. Nature Methods **20**(8), 1183–1186 (2023) https://doi.org/10.1038/s41592-023-01958-0

[27] Lefkimmiatis, S., Bourquard, A., Unser, M.: Hessian-based norm regularization for image restoration with biomedical applications. IEEE Transactions on Image Processing **21**(3), 983–995 (2012) https://doi.org/10.1109/TIP.2011.2168232

[28] Yang, X., Zhu, H., Sun, Y., Wu, H., Han, Y., Hao, X., Kuang, C., Liu, X.: Accurate 3d single-molecule localization via vectorial *in situ* point spread function retrieval and aberration assessment. Photonics Research **12**(11), 2447–2461 (2024) https://doi.org/10.1364/PRJ.520469

[29] Thao, N.H., Soloviev, O., Verhaegen, M.: Phase retrieval based on the vectorial model of point spread function. JOSA A **37**(1), 16–26 (2020) https://doi.org/10.1364/JOSAA.37.000016

[30] Huang, F., Sirinakis, G., Allgeyer, E.S., Schroeder, L.K., Duim, W.C., Kromann, E.B., *et al.*: Ultra-high resolution 3d imaging of whole cells. Cell **166**(4), 1028–1040 (2016) https://doi.org/10.1016/j.cell.2016.06.016

[31] Boyd, S.: Distributed optimization and statistical learning via the alternating direction method of multipliers. Foundations and Trends® in Machine Learning **3**(1), 1–122 (2010) https://doi.org/10.1561/2200000016